Corrosion Science 78 (2014) 188–192

Contents lists available at ScienceDirect

Corrosion Science

journal homepage: www.elsevier.com/locate/corsci

Thermogravimetry and insitu mass spectrometry at high temperatures compared to thermochemical modelling – The weight loss during selective decarburisation at 800 °C

M. Auinger [a,c,*], A. Vogel [a], V.G. Praig [b,c], H. Danninger [b,c], M. Rohwerder [a,c]

[a] Max-Planck-Institut für Eisenforschung GmbH, Max-Planck-Straße 1, D-40237 Düsseldorf, Germany
[b] Institute of Chemical Technologies and Analytics, Vienna University of Technology, Getreidemarkt 9, A-1060 Vienna, Austria
[c] Christian Doppler Laboratory for Diffusion and Segregation Phenomena during the Production of High Strength Steel Sheets

ARTICLE INFO

Article history:
Received 3 April 2013
Accepted 29 September 2013
Available online 12 October 2013

Keywords:
A. Steel
B. Modelling studies
B. Weight loss
C. High temperature corrosion
C. Selective oxidation
Thermogravimetry and insitu mass spectrometry

ABSTRACT

The insitu mass spectrometry detection of volatile species during high temperature corrosion processes, exemplified by decarburisation of plain carbon steel, will be presented. Without influencing the thermobalance signal, changes of the gas composition can be measured by introducing a small quartz capillary into the reaction chamber in close proximity to the sample surface.

Experiments with the eutectoid composition Fe, 0.8 wt% C have been chosen intentionally as this alloy represents one of the most intensely studied compositions in steel research. This allows good verification with commonly accepted knowledge. Furthermore, comparison between experimental observations and theoretical simulations will be given and critically discussed.

1. Introduction

A detailed understanding of high temperature corrosion processes is of vital importance for many industrial applications such as waste incineration [1] and power generation [2]. Additionally, the utilisation of new energy sources demands for new, corrosion-protective materials [3,4] and represents an important challenge for the near future. Throughout the past decades, remarkable efforts have been made in this research discipline [5–7] yielding sound descriptions of the mechanisms for high temperature oxidation [8–10] and nitridation [11] in metals or their reaction with strongly segregating elements like phosphorus, sulfur [12] and boron. Apart from classical corrosion processes where reactive gas species move into the material and form new phases [13–15], the reverse process (i.e. the volatilisation of a materials component [16,17]) may also lead to materials degradation.

Beside a detailed description of the origin of failure, reliably predicting the tendency of a material to form high temperature corrosion products and, hence maybe, circumventing long-term exposure tests of up to several thousand hours is still a challenge for modern corrosion scientists. Numerical modelling has proven to be extremely valuable and many studies on the combination of diffusion processes with chemical equilibrium reactions have been published so far [18–20]. To complement such calculations, it is the aim of this work to give a comparison between experimental results and theoretical findings. The eutectoid mixture of iron with 0.8 wt% carbon (typically with pearlitic microstructure) was chosen for the samples under investigation, since this composition is among the most intensely studied binary alloys [22,23]. Furthermore, decarburisation effects can easily be detected by optical microscopy, owing to emergence of the bright ferrite. A detailed description of decarburisation depth and mass loss will be given, based on theory (numerical modelling) as well as based on the experimental results. Furthermore, the insitu detection of the gas composition near the sample surface during heat exposure will be presented.

2. Experimental

For measurements of the decarburisation depth, the cast alloy Fe, 0.8 wt% C (ingot, produced in house) was cut into square shaped pieces of 15 mm × 15 mm × 4 mm in size. A small hole was drilled on one front face, where the sample was mounted on the thermocouple. Samples for thermogravimetry were prepared with dimensions of 10 mm × 10 mm × 1 mm and a small hole was drilled to mount the sample on the quartz hook of the thermobalance. All

* Corresponding author at: Max-Planck-Institut für Eisenforschung GmbH, Max-Planck-Straße 1, D-40237 Düsseldorf, Germany. Tel.: +49 (0)211 6792 884.
E-mail address: auinger@mpie.de (M. Auinger).

0010-938X/$ - see front matter © 2013 Elsevier Ltd. All rights reserved.
http://dx.doi.org/10.1016/j.corsci.2013.09.015

surfaces of the samples were mechanically polished by using grinding papers from 400 down to 2500 grit size and were ultrasonically cleaned in ethanol.

Selective decarburisation experiments were carried out at 800 °C for up to 120 min in an infra-red heated furnace equipped with a thermobalance, as illustrated in Fig. 1.

A mixture of Ar/H_2 (97.5/2.5, v/v) with a total gas flow of 30 l h^{-1} was used. The humidity of the gas mixture was chosen to be +13 °C dew point (15000 ppm H_2O), which yields an oxygen activity just below the thermodynamic onset of wustite formation under these conditions (+15.4 °C dew point). Great care has been taken to reduce the content of oxygen impurities below a limit of 5 ppm O_2. All process parameters (temperature, gas composition, mass signal) during heat exposure were recorded automatically and stored in a single text file [24]. The insitu mass spectrometry measurements (GAM 200, InProcess Instruments) of CO_x, H_2, H_2O and Ar were obtained by using a small fused quartz capillary (InProcess Instruments, Germany) which was introduced into the reaction chamber in close proximity of less than 1 mm to the sample surface during heat exposure. After decarburisation, the samples were cross-sectioned and etched in 1% HNO_3/ethanol for 15 s to better visualise the carbon rich phases.

3. Simulations

Numerical simulations of the phase distributions were calculated by a subsequent two-step based algorithm, consisting of element migration and thermodynamic reactions [21]. Transport of the atomic species (oxygen and carbon) has been derived from the set of partial differential equations and assuming the diffusion coefficients to be dependent on the molar fraction of ferrite and austenite, according to the iron–carbon phase diagram [25]. The oxygen concentration at the surface (upper boundary) is set as constant, according to the maximum solubility of oxygen under given temperature and partial pressure. This corresponds to the constant source model, firstly proposed by Fisher [26]. Oxygen would have to firstly diffuse through the decarburised (alpha iron) zone before reaching the carbon-rich austenite phase. Multiplying the diffusivity coefficient of oxygen in ferrite ($D = 6.56 \times 10^{-11}$ m^2 s^{-1} [27]) with its solubility, we obtain an oxygen permeability of 4.58×10^{-16} m s^{-1} molO $molFe^{-1}$. This is considerably lower than the carbon permeability [28] in ferrite (1.36×10^{-13} m s^{-1} molC $molFe^{-1}$) and in austenite (5.76×10^{-14} m s^{-1} molC $molFe^{-1}$), leading to the conclusion that carbon transport in the ferrite zone is the fastest and the carbon monoxide formation during decarburisation must occur at the sample surface. Insulating boundary conditions for the element transport were set at a depth of 0.5 mm, to account for the expected symmetry of the concentration distributions and mimicking a total sample thickness of 1 mm, which have been used for the thermogravimetry experiments.

The calculation of the diffusion has been carried out for small time intervals. The results after each calculation step have been used to derive the local concentrations of each phase with the thermodynamic subroutine ChemApp (GTT-Technologies, Germany). The amount of each phase from the equilibrium calculation was set as the starting value for the diffusion calculation in the next time step. After the last simulation step, the results were displayed as a one-dimensional concentration map – similar to a line scan of a cross sectioned specimen – indicating the amount and spatial distribution of each phase.

Results of the thermogravimetry behaviour have been derived by integrating the total amount of carbon in the sample and converting the molar amounts into a mass signal by using the density of austenite at 25 °C (ρ = 7.692 g cm^{-3} [29]) to obtain the total volume of the sample.

4. Results and discussion

Very stable conditions for sample temperature and gas humidity could be achieved, as illustrated in Fig. 2. Oxygen contents in the reaction gas were always below 5 ppm and decreased even further at rising temperature (see Fig. 2 left), as some oxygen impurities begin to react with either carbon or hydrogen. Due to the rapid heating up to 800 °C, the mass signal behaves randomly within the first 5 min. This behaviour may be attributed to buoyancy effects of the sample in a highly unstable gas stream which dominates the initial stages of the measurement. A continuous decrease of the observed mass signal can be seen during the experiment, which is a clear indication of the decarburisation process. Simultaneously, the formation of carbon monoxide occurs which is most

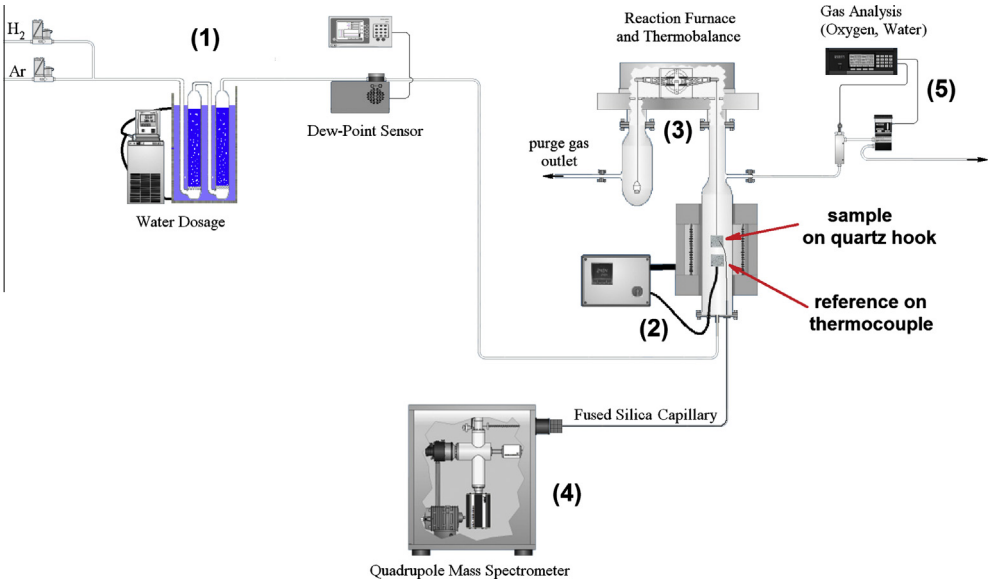

Fig. 1. Experimental set-up for in-situ thermogravimetry and mass spectrometry, showing a gas conditioning unit (1), an infra-red furnace (2) with themobalance (3), in-situ mass spectrometry (4) and additional oxygen sensors (5). Further details of the experimental set-up can be found in [24].

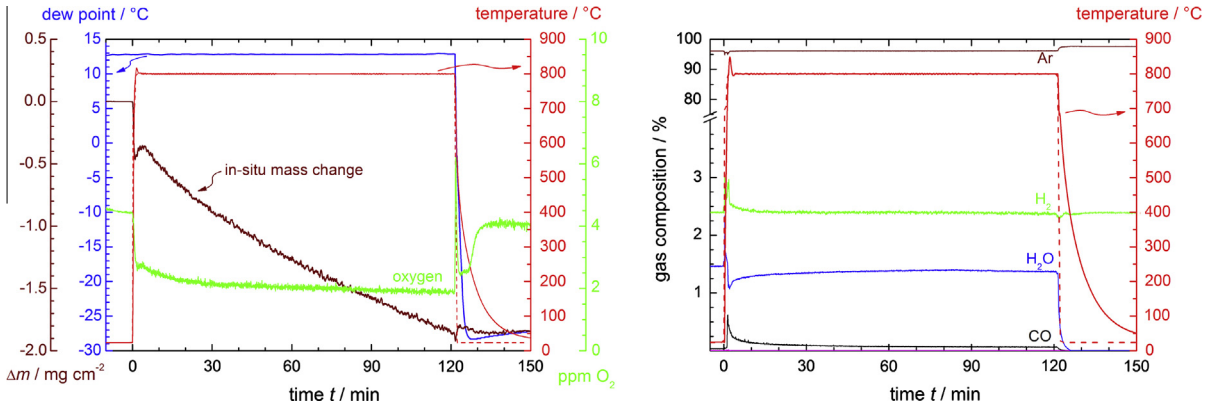

Fig. 2. Thermogravimetry (left) and in-situ mass spectrometry of the reaction gas composition near the sample surface (right) during heat treatment of Fe, 0.8 wt% C, oxidised at 800 °C for 120 min in Ar/2.5% H_2/H_2O (15000 ppm, DP + 13 °C, $p(O_2) = 10^{-19}$ bar). The dashed line in both graphs represents the set-temperature programme.

pronounced in the initial stages of the decarburisation process and quickly drops down with time, as shown in the mass spectrometry curves in Fig. 2 (right). Remarkably, a significant decrease of the humidity and an increase of the hydrogen signal in close proximity to the sample surface could be observed in all measurements. Although these changes are very difficult to be measured with a normal equipment for measuring the bulk gas composition – the sample (reactive surface) is very small compared to the total volume of the reaction chamber – these changes become clear, since oxygen needs to be provided from water vapour to form carbon monoxide, according to $C + H_2O \rightarrow CO + H_2$ [30].

Cross sectional images indicate that the decarburised samples are composed of three different zones. The topmost (decarburised) zone comprises of huge ferrite grains of a rod-like shape, as decarburisation and the resulting austenite-ferrite transformation starts at the surface and self diffusion in the alpha iron lattice is very large compared to austenite [28], which leads to fast defect migration and grain growth. The innermost zone contains the nominal composition of the bulk material and shows the typical fine-lamellar structure of pearlite. An intermediate layer contains both, ferritic grains and small pearlite islands, which indicates material that has been partially decarburised but has still been austenitic at processing temperature. Fig. 3 illustrates the results.

The time dependence of the decarburisation depth in Fig. 4 follows the same trend as the observed thermogravimetric signal from Fig. 2. In the beginning of the heat exposure, the thickness of the decarburised zone increases a little bit faster and gradually slows down with longer exposure times. Again, three different zones can be clearly distinguished. Although the rod like structure of the ferritic zone does exist in the heated samples, it cannot be seen, because the cross sections were prepared with a 7° tilt angle to the surface, compared to 90° in Fig. 3. This preparation cuts the ferrite rods almost perpendicularly to their growth axis, and they appear virtually equiaxed. After an exposure of 120 min, the depth of the decarburisation zone is around 275 μm, compared to 110 μm after 15 min.

Numerical simulations [21] have been carried out to verify the experimental findings with theoretical knowledge from solubility and diffusivity data available in the literature [27,28]. Phase distributions were assumed to be in local thermodynamic equilibrium and the decarburisation process (i.e. in this case the resulting austenite–ferrite transformation) is not obstructed by reaction kinetics. Diffusion of carbon in the material has been calculated by using bulk diffusion coefficients at 800 °C in ferrite ($D = 2.44 \times 10^{-10}$ m^2 s^{-1} [28]) and austenite ($D = 1.49 \times 10^{-12}$ m^2 s^{-1} [28]) without taking the effect of grain boundaries into account. Although a fine ensemble of randomly oriented grain boundaries can be seen in the pearlite zone in Fig. 3, it seems unlikely that this structure already exists during thermal exposure since the samples should be completely austenitic at 800 °C. The ordered columnar grain structure in the ferrite zone may have an influence on carbon diffusion. However, published values for grain boundary diffusion coefficients of carbon in ferrite

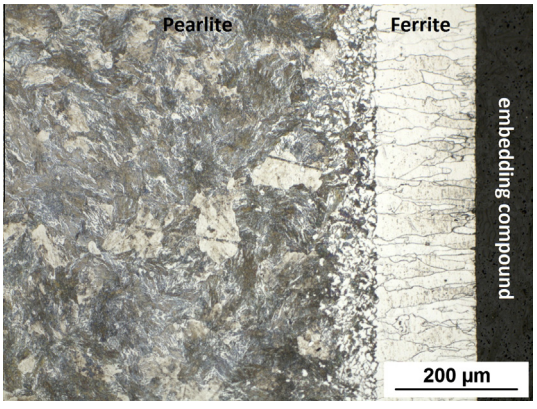

Fig. 3. Cross section of an Fe, 0.8 wt% C sample after annealing at 800 °C in Ar/2.5% H_2/H_2O (15000 ppm, DP + 13 °C, $p(O_2) = 10^{-19}$ bar) for 60 min. The cross section was etched with 1% HNO_3/Ethanol for 15 s.

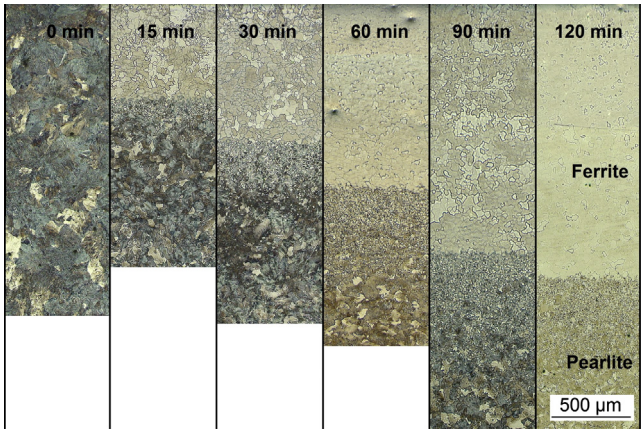

Fig. 4. Light optical microscopy of Fe, 0.8 wt% C samples after annealing at 800 °C in Ar/2.5% H_2/H_2O (15000 ppm, DP + 13 °C) for different times. After the treatment, the samples were cut and ground in a 7° tilt angle to the surface. The samples were polished with 1 μm diamond paste and etched with 1% HNO_3/Ethanol for 15 s.

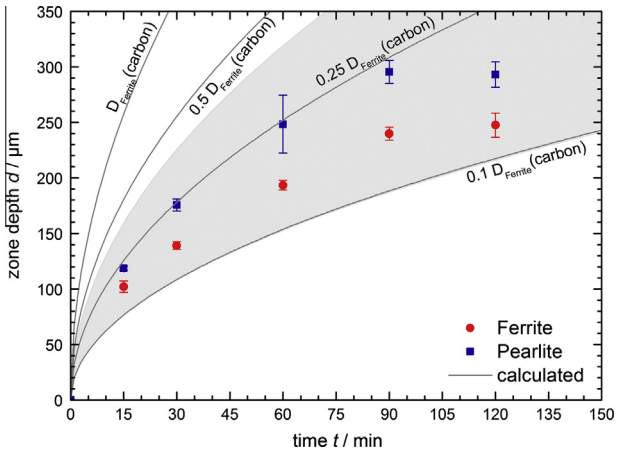

Fig. 5. Evolution of the decarburised zone depth in Fe, 0.8 wt% C, after annealing at 800 °C in Ar/2.5% H_2/H_2O (15000 ppm, DP + 13 °C, $p(O_2) = 10^{-19}$ bar). The solid lines represent the theoretical results at 50% decarburisation with different deceleration factors (1, 0.50, 0.25, 0.10) for carbon diffusion in an ideal ferrite crystal. Grey shaded areas mark the distance between 25% and 75% ferrite in the material for the deceleration factor 0.25.

differ by several orders of magnitude [28,31,32] and may depend on the grain boundary orientation which is not uniform during thermal exposure.

As the effect of microstructural changes and reaction kinetics cannot be covered by a reaction-diffusion based model without the use of additional parameters like recrystallisation rate and energy values for grain boundary interfaces or activation barriers for chemical reactions, the transition region between bulk material and decarburised zone appears to be larger in the simulations than in experiments. The calculated depth of the decarburised zone, as shown in Fig. 5, is defined by the presence of 50% of the initial carbon concentration. Overall, good agreement between theoretical results and experimental findings could be verified when assuming the effective carbon diffusion to be decreased by a factor of 0.10–0.25 compared to the ideal ferrite crystal. This decrease may be attributed to the convolute effect of austenite decomposition kinetics [33] and the ordered microstructure in the ferrite zone.

Additionally, the simulated mass loss during heat exposure in Fig. 6 can be successfully described by using the same values from literature as already used for the description of the decarburisation

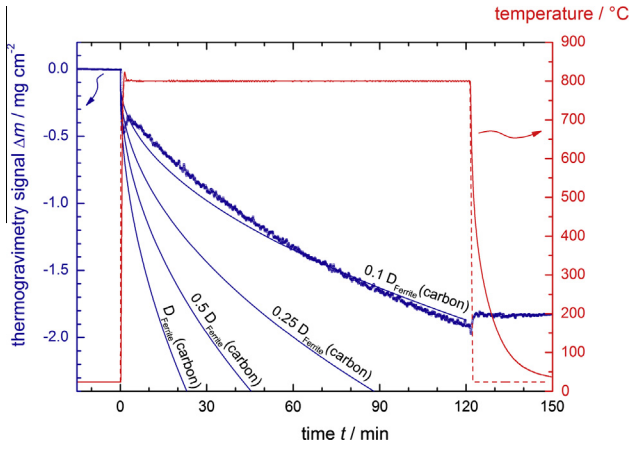

Fig. 6. Comparison between the experimental data, shown in Fig. 2 and the simulated mass loss with different deceleration factors (1, 0.5, 0.25, 0.10) for carbon diffusion in an ideal ferrite crystal (solid lines). The experimental data was obtained by insitu thermogravimetry (□) during decarburisation of Fe, 0.8 wt% C at 800 °C in Ar/2.5% H_2/H_2O (15000 ppm, DP + 13 °C, $p(O_2) = 10^{-19}$ bar).

depth. Good agreement between theory and experiment could be verified by applying a deceleration factor of 0.10 for carbon diffusion, which is in agreement with the results from Fig. 5. This is an additional verification of the parameters used for diffusion and solubility of both, carbon and oxygen and leads to the consequence that decarburisation in the samples appears to be uniform and will not be locally enhanced or retarded. Furthermore, the necessity of a deceleration factor (often described as "effective" diffusion coefficient) indicates that phase transformations and sample microstructure can lead to severe differences between known results from single phases and observations for polycrystalline materials.

Sudden drops of the measured mass signal during rapid heating were taken into account in the simulations by subtracting the mass change of the sample during the cooling step. The resulting deviation between theory and experiment within the first 5 min of the exposure are indeed caused by buoyancy effects of the thermobalance set-up.

5. Conclusions

Selective oxidation of carbon at 800 °C in an environment of Ar/H_2 with defined humidity and low oxygen activity has been investigated for eutectoid iron–carbon samples (pearlitic microstructure). The observed mass loss during heat exposure quickly stabilises after an initial irregular, buoyancy-dominated period, caused by the rapid heating step. The microstructure of the decarburised samples shows three different zones: rod-like ferrite grains near the surface, an intermediate layer of ferrite and pearlite and pearlite in the bulk.

Theoretical simulations were carried out by using tabulated literature values for diffusion and solubilities as well as applying local thermodynamic equilibrium conditions of the reacting species, oxygen and carbon. Good agreement with experimental results could be verified when assuming a deceleration factor of 0.1 for the carbon diffusion in ferrite, which may originate from the convolute effect of slow austenite decomposition kinetics and carbon diffusion in the oriented grain boundary structure of the top-most ferrite zone. Discrepancies between experimental findings and theoretical expectations clearly show, that numerical simulations have to be carried out with greatest care in the selection of used datasets, the definition of assumptions and the interpretation of results rather than performing calculations on a goodness-of-fit base.

Additionally, insitu mass spectrometry measurements of the reaction gases in close proximity to the sample surface were performed, which further document the decarburisation behaviour and meet highest standards in high temperature corrosion research.

It needs to be emphasised that the system iron–carbon has been chosen intentionally for these studies as it represents a generic system for more complex steel compositions. Furthermore, pearlite counts amongst the most intensely studied alloy compositions and hence provides a good comparison with other sources from literature to the critical reader. For metallographic characterization, a fully pearlitic microstructure is well suited to reveal local decarburisation effects since the emergence of ferrite is immediately visible.

Acknowledgements

The authors are thankful to Dr. Dieter Paesold, Dr. Bernhard Linder and Dr. Wolfgang T. König (all voestalpine Stahl GmbH) for helpful discussions. Financial support by the Christian Doppler Society (Austria) and the voestalpine Stahl GmbH (Austria) is gratefully acknowledged.

References

[1] M. Spiegel, H.J. Grabke, High temperature corrosion of high alloy steels in simulated waste incineration environments, Mater. Corros. 47 (1996) 179–189.
[2] A.U. Syed, N.J. Simms, J.E. Oakley, Fireside corrosion of superheaters: Effects of air and oxy-firing of coal and biomass, Fuel 101 (2012) 62–73.
[3] B.A. Pint, Y. Zhang, P.F. Tortorelli, J.A. Haynes, I.G. Wright, Evaluation of iron-aluminide CVD coatings for high temperature corrosion protection, Mater. High Temp. 18 (2001) 185–192.
[4] H. Nickel, W.J. Quadakkers, L. Singheiser, Determination of corrosion layers and protective coatings on steels and alloys used in simulated service environment of modern power plants, J. Press. Vess.-T. ASME 128 (2006) 130–139.
[5] T. Gheno, D. Monceau, J. Zhang, D.J. Young, Carburisation of ferritic Fe-Cr alloys by low carbon activity gases, Corros. Sci. 53 (2011) 2767–2777.
[6] A. Ollivier-Leduc, M.-L. Giorgi, D. Balloy, J.-B. Guillot, Nucleation and growth of selective oxide particles on ferritic steel, Corros. Sci. 52 (2010) 2498–2504.
[7] B. Pujilaksono, T. Jonsson, M. Halvarsson, J.-E. Svensson, L.-G. Johansson, Oxidation of iron at 400–600°C in dry and wet O_2, Corros. Sci. 52 (2010) 1560–1569.
[8] R.Y. Chen, W.Y.D. Yuen, Review of the high-temperature oxidation of iron and carbon steels in air or oxygen, Oxid. Met. 59 (2003) 433–468.
[9] A.L. Marasco, D.J. Young, The oxidation of iron–chromium–manganese alloys at 900°C, Oxid. Met. 36 (1991) 157–174.
[10] P.R. Wilson, Z. Chen, The effect of manganese and chromium on surface oxidation products formed during batch annealing of low carbon steel strip, Corros. Sci. 49 (2007) 1305–1320.
[11] P.C. Van Wiggen, H.C.F. Rozendaal, E.J. Mittemeijer, The nitriding behaviour of iron–chromium–carbon alloys, J. Mater. Sci. 20 (1985) 4561–4582.
[12] H.J. Grabke, Surface and grain boundary segregation an and in iron and steels, ISIJ Int. 29 (1989) 529–538.
[13] L. Lui, Z.-G. Yang, C. Zhang, M. Ueda, K. Kawamura, T. Maruyama, Effect of water vapour on the oxidation of Fe–13Cr–5Ni martensitic alloy at 973 K, Corros. Sci. 60 (2012) 90–97.
[14] H. Yedong, F.H. Stott, The effects of thin surface-applied oxide coating films on the selective oxidation of alloys, Corros. Sci. 38 (1996) 1853–1868.
[15] H. Li, Y. Zheng, L.W. Benum, M. Oballa, W. Chen, Carburization behaviour of Mn–Cr–O spinel in high temperature hydrocarbon cracking environment, Corros. Sci. 51 (2009) 2336–2341.
[16] H. Asteman, J.-E. Svensson, L.-G. Johansson, Oxidation of 310 steel in H_2O/O_2 mixtures at 600 °C: the effect of water–vapour-enhanced chromium evaporation, Corros. Sci. 44 (2002) 2635–2649.
[17] D. Li, D. Anghelina, D. Burzic, J. Zamberger, R. Kienreich, H. Schifferl, W. Krieger, E. Kozeschnik, Investigation of decarburisation in spring steel production process – part i: experiments, Steel Res. Int. 80 (2009) 298–303.
[18] T.J. Nijdam, L.P.H. Jeurgens, W.G. Sloof, Modelling the thermal oxidation of ternary alloys – compositional changes in the alloy and the development of oxide phases, Acta Mater. 51 (2003) 5295–5307.
[19] W.M. Pragnell, H.E. Evans, A finite-difference model to predict 2D depletion profiles arising from high temperature oxidation of alloys, Modelling Simul. Mater. Sci. Eng. 14 (2006) 733–740.
[20] D. Li, D. Anghelina, D. Burzic, W. Krieger, E. Kozeschnik, Investigation of decarburisation in spring steel production process – part ii: simulation, Steel Res. Int. 80 (2009) 304–310.
[21] M. Auinger, R. Naraparaju, H.J. Christ, M. Rohwerder, Modelling high temperature oxidation in iron–chromium systems: combined kinetic and thermodynamic calculation of the long-term behaviour and experimental verification, Oxid. Met. 76 (2011) 247–258.
[22] H.J. Grabke, M. Schütze, Corrosion by Carbon and Nitrogen: Metal Dusting, Carburisation and Nitridation, 41st ed., Woodhead and Maney for European Federation of Corrosion, 2007.
[23] D. Young, High Temperature Oxidation and Corrosion of Metals, 1st ed., Elsevier, Oxford, 2008.
[24] M. Auinger, D. Vogel, A. Vogel, M. Rohwerder, M. Spiegel, A novel laboratory set-up for investigating surface and interface reactions during short term annealing cycles at high temperatures, Rev. Sci. Instr. 84 (2013) 085108.
[25] B.L. Bramfitt, A.O. Benscoter, Metallographer's Guide – Practice and Procedures for Irons and Steels, 1st ed., ASM International, Materials Park Ohio, 2002.
[26] J.C. Fisher, Calculation of diffusion penetration curves for surface and grain boundary diffusion, J. Appl. Phys. 22 (1951) 74–77.
[27] H.J. Swisher, E.T. Turkdogan, Solubility, permeability, and diffusivity of oxygen in solid iron, T. Metall. Soc. AIME 239 (1967) 426–431.
[28] H. Mehrer, Landolt Börnstein – Numerical Data and Functional Relationships in Science and Technology: Group III, vol. 26, Springer, Berlin, 1990.
[29] Y.N. Osetsky, A. Serra, Computer-simulation study of high-temperature phase stability in iron, Phys. Rev. B 57 (1998) 755–763.
[30] R. Yin, Thermodynamic roles of metallic elements in carburization and metal dusting, Oxid. Met. 61 (2004) 323–337.
[31] E. Budke, C. Herzig, H. Wever, Volume and grain boundary diffusion of ^{14}C in a-Fe, Phys. Stat. Sol. 127 (1991) 87–101.
[32] I. Kaur, Y. Mishin, W. Gust, Fundamentals of grain and interphase boundary diffusion, 3rd ed., John Wiley & Sons Ltd., New York, 1995.
[33] R.A. Vandermeer, Modelling diffusional growth during austenite decomposition to ferrite in polycrystalline Fe–C alloys, Acta Metall. Mater. 38 (1990) 2461–2470.